Microwave-driven carbonation of brucite

Marcello Campione [a,*], Mattia Corti [a], Daniela D'Alessio [a], Giancarlo Capitani [a], Andrea Lucotti [b], Rossella Yivlialin [c], Matteo Tommasini [b], Gianlorenzo Bussetti [c], Nadia Malaspina [a]

[a] Department of Earth and Environmental Sciences, University of Milano - Bicocca, Piazza della Scienza 4, I-20126 Milano, Italy
[b] Department of Chemistry, Materials and Chemical Engineering, Politecnico di Milano, Piazza Leonardo da Vinci 32, I-20133 Milano, Italy
[c] Department of Physics, Politecnico di Milano, Piazza Leonardo da Vinci 32, I-20133 Milano, Italy

ABSTRACT

The water-mediated mineral carbonation represents a promising solution for the capture and the storage of atmospheric CO_2. Even though this reaction might be spontaneous for a number of Mg- and Ca-rich mineral phases, it is characterized by considerable activation barriers. In order to make it effective, associated energy costs related to the achievement of adequate reaction conditions must be minimized. Microwave chemistry is known to provide for substantial increments of the reaction rate for several systems. We applied here microwave chemistry to the process of carbonation of aqueous slurries of brucite, a model system of Mg-rich mineral, subjected to partial pressures of CO_2 as low as 6 bar and to no other additive. The temperature of the reactor was finely varied while the radiation power and the reactor pressure were monitored in real-time. The radiation power was used to estimate the radiation energy budget needed to complete the carbonation process, whereas the reactor pressure was used as a proxy of reaction progression. We show a detailed evolution of the carbonate products obtained in terms of mineral phases, morphological properties, and degree of crystallinity, both as precipitate and as solid residue in the exsiccated supernatant reaction liquid.

1. Introduction

During the last two centuries, the average concentration of CO_2 in the troposphere has undergone a nearly 50% increment, passing from 280 ppm at the end of the 18th century, to 410 ppm today [1]. This increment has been recognized as being significantly influenced by anthropic activities and responsible for a substantial enhancement of the greenhouse effect causing a steady positive drift of average temperatures around the globe.

Mitigation actions are developing along two main routes: a) the reduction of CO_2 emissions related to the combustion of fossil fuels, and b) CO_2 capture from the troposphere for its utilization or permanent storage (CCUS) [2]. Route a) determines primarily the definition of proper policy choices aimed at discouraging energy consuming behaviours and incentivizing the deployment of removable energy sources, whereas route b) is boosting scientific research in cross-disciplinary fields. For instance, the combination of physical and chemical processes enables CCUS to involve the transformation of the greenhouse gas into other compounds, which sometimes possess a value as secondary raw materials. In this regard, chemical methods can be employed to

reduce CO_2 into organic compounds (*e.g.*, methanol and oxalates) [3]; otherwise, CO_2 can be used as acid reactant to form insoluble salts with basic rocks (*e.g.*, basalts). This latter process occurs in natural weathering of rocks, where Mg- and Ca-rich silicates are slowly leached by the action of CO_2-saturated water to produce insoluble carbonates [4,5]. The implementation of enhanced forms of weathering to harness the water-mediated carbonation reaction for realizing sustainable and scalable processes of CCUS takes advantage of a series of technological solutions, which are aimed at controlling the reaction kinetics of a heterogeneous phase composed by a solid (the rock), a liquid (water) and a gas (CO_2). Reaction rate increments can be accomplished by adopting elevated temperature-pressure conditions [6], or by implementing activating heat treatments [7] and grinding processes [8]. However, these solutions might result energy-intensive, coming into conflict with the need to ensure low process costs and energy demand, in compliance with the requirements of circular economy. For this reason, alternative processes are being developed with the aim of providing energy efficiency and reducing reaction times [9]. A valuable model of solid phase for the study of carbonation reactions is represented by magnesium hydroxide, a system made up of only two components (MgO

---

* Corresponding author.
E-mail address: marcello.campione@unimib.it (M. Campione).

+ H_2O) occurring in nature in the form of brucite mineral. Brucite can be also considered as a proxy of other very abundant Earth minerals, such as serpentine [$Mg_3Si_2O_5(OH)_4$], which is composed by the alternation of brucite-like and silicate layers, representing potential reservoirs for the accomplishment of large-scale CCUS, with significant positive impact for the environment [10–12]. The products of the water-mediated carbonation of Mg-rich rocks are magnesium hydroxy-carbonate hydrates (MHCH) and magnesite ($MgCO_3$). Within the framework of long term CCUS, it is noteworthy that MHCH tend to decrease their water content with time, transforming into magnesite, the thermodynamically most stable and densest form of Mg-carbonate [13]. From another standpoint, MHCH represent, like $MgCO_3$, valuable secondary materials with application as construction products [14].

In the experimental study of water-mediated carbonation of brucite, a slurry of the powdered mineral is prepared and maintained at a certain temperature while injection in the reactor of the CO_2-containing gas is carried out at various pressures. Recent studies show that, by conventional thermal heating, the product of brucite carbonation can be varied, passing from nesquehonite [$Mg(HCO_3)(OH)·2H_2O$] at low temperature (< 50 °C) [15], hydromagnesite [$Mg_5(CO_3)_4(OH)_2·4H_2O$] at intermediate temperatures (150 °C), and magnesite at high temperature (> 200 °C) [16]. In these studies, CO_2 partial pressure is maintained at 15 bar and steadily pressing into the reactor. The reaction kinetics is inferred by the measurement over time of the fraction of carbonate phase in the precipitated solid and the concentration of ionic species in the liquid phase.

Here, we applied for the first time microwave (MW) heating for driving the carbonation reaction of brucite in a reactor allowing for the fine real-time control of temperature, pressure, and radiation energy spent. The use of MW, while generally makes the heating process more efficient with respect to conventional convective heat transfer, contributes to the enhancement of the water-mediated carbonation because of the augmentation of the diffusion coefficient of reactive electrolytes [17], boosting both dissolution (*i.e.*, acid digestion) and liquid to solid mass transfer (*i.e.*, crystallization) processes [17–21]. In fact, brucite carbonation comprises three steps:

gas dissolution in water:
$$CO_{2,g} = CO_{2,aq}; \quad CO_{2,aq} + H_2O = H_2CO_{3,aq} \tag{1}$$

acid dissolution of brucite:
$$Mg(OH)_{2,s} + H_2CO_{3,aq} = Mg^{2+}_{aq} + CO^{2-}_{3,aq} + 2H_2O \tag{2}$$

carbonate precipitation:
$$Mg^{2+}_{aq} + CO^{2-}_{3,aq} = MgCO_{3,s} \tag{3}$$
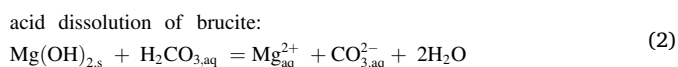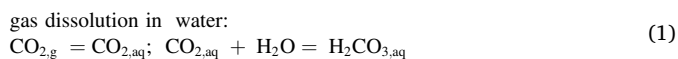
Reaction (1) is influenced by the solution pH. Since brucite slurries are slightly alkaline (pH $\approx$10 at 23 °C), gas dissolution is enhanced by the onset of the reaction: $CO_{2,aq} + OH^-_{aq} = HCO^-_{3,aq}$ [22].

While reaction (1) might be insensitive to the presence of the electromagnetic perturbation given by MW, reactions (2) and (3) are expected to be substantially accelerated. In this regard, the enhancement of the precipitation rate of Mg- and Ca-carbonates with the application of MW radiation was demonstrated [23–25]. It must be noted that reactions (2) and (3) are mutually influenced, since carbonates might precipitate on the surface of residual brucite, giving rise to passivation effects.

We explored a temperature range from 40 to 220 °C, with intervals of 15 °C (plus the additional data acquired at room temperature (RT), about 23 °C), while using CO_2 partial pressures as low as 6 bar in a 50% mixture with N_2, and injected only at the beginning of the treatment, without the addition of any other chemical additive. The pressure monitored in real-time is adopted as a reaction kinetic-related parameter to infer reaction rates and to determine times for reaction completion. We systematically analysed both the final precipitate products and the solid residue of the liquid phase by X-ray diffraction, vibrational

spectroscopy, and electron microscopy, enabling us to identify the chemical nature of the products, their crystallinity, and to provide mass yields and energy costs as a function of temperature.

2. Materials and methods

Each carbonation run consisted in the preparation of a brucite (Sigma-Aldrich) slurry containing *ca.* 5.5 g (0.094 mol) of solid suspended in 300 ml of deionized water. The solid investigated by scanning electron microscopy (SEM, *vide infra*) occurs as spherulitic aggregates of about 50 μm of diameter composed by nanometric plate-like crystallites (Fig. S1). Brucite dispersion was accomplished by the aid of a sonication treatment of about 5 min. Scherrer analysis (*vide infra*) of the pristine brucite powder provided an average size of crystal domains of (36.3 $\pm$ 1.2) nm, whereas dynamic light scattering analysis of the slurries provided an estimation of the size of suspended aggregates of the order of 1 μm. Carbonation of the slurry was performed through a MW synthesizer (SynthWave, Milestone) equipped with a Teflon-lined reactor with capacity of 900 ml. The reactor containing the slurry was pressurized at RT through injection of 6 bar of CO_2 (99.995%) and 6 bar of N_2 (99.999%), as measured by a built-in pressure gauge. The quantity of injected CO_2 can be estimated by the ideal gas equation of state to be 0.15 mol, which represents a 50% excess quantity with respect to the one required to neutralize all the brucite charge. The mixture with N_2 and the relatively low partial pressures adopted had the scope to use the CO_2 reactant in a dilute form and under conditions easily scalable and close to those available at industrial contexts (*e.g.*, fuel gas). Gas charging at RT before heating onset instead of gas injection at the setpoint temperature was chosen to allow us to use the measured pressure as a parameter to monitor CO_2 capture rates and to explore high temperature ranges, where vapor pressures overcome 25 bar and gas ignition through ordinary gauges becomes impossible. Reaction runs started with a linear heating ramp lasting 600 s (except the RT run, carried out with no MW irradiation) until the achievement of the setpoint temperature, as measured by a temperature gauge immersed in the slurry. Once the setpoint temperature was reached, a dwelling stage started and lasted 2 h for treatments up to 145 °C, and 1 h for treatments from 160 to 220 °C. Setpoint temperatures ranged from 40 to 220 °C, with intervals of 15 °C. After completion of the run, the reactor was cooled down by a water circuit running inside the reactor steel chamber. Decompression of the reactor was undertaken at a temperature below 65 °C and opening of the reactor chamber was carried out at a temperature below 45 °C.

Parallel reference treatments were performed with deionized water without any solid charge and a water slurry with 5.5 g of talc (Fischer Scientific), to test the effect of sole CO_2 dissolution and the presence of a far less reactive suspended magnesium silicate on the pressure trend during MW treatments.

The reactor content after each run was transferred in a set of centrifuge vials and centrifugation was performed at 6000 rpm with duration of 5 min, for separating the solid precipitate from the supernatant solution. The precipitates were analysed after exsiccation at a temperature of 40 °C for 24 h. The supernatant solutions were dried at 40 °C or higher temperature, though inferior to the setpoint value, for investigating the effect of temperature on the composition and structure of the solid residues obtained. Powder X-ray Diffraction (PXRD) of the solid products was carried out with a Bragg-Brentano geometry Panalytical X'Pert Pro Diffractometer (Malvern Panalytical), using CuK_α radiation (1.5417 Å, 40 kV and 40 mA), and a divergence slit of 1/2°. The powder samples were back-loaded on a flat sample-holder, and PXRD patterns were collected over a 2θ angular range of 5–80°, with 0.0167° per step and a counting time of 90 s/step. Qualitative analyses were preliminary done employing *Match!* software, and then the phase amounts were evaluated from PXRD patterns by means of the full profile Rietveld Refinement Method [26], implemented in GSAS software, and with EXPGUI as graphical interface [27]. The micro-Raman

measurements were carried out with the LABRAM HR800 instrument (Horiba Jobyn-Yvon) using a 50X objective (0.75 NA, laser spot size about 1 μm) and the 405 nm excitation provided by a solid-state laser produced by Integrated Optics. Before measurements, the sample powder was gently pressed on a microscope glass slide. For each different point on the powder sample, the laser focusing procedure was repeated before collecting the Raman spectra. The different points on the sample were randomly selected within a zone of a few millimetres in diameter. For each sample in powder form, we collected several spectra (a minimum of 3, up to 11, depending on the spatial inhomogeneity) by focusing the laser on points of the sample. The reference spectra of hydromagnesite, magnesite, and nesquehonite were taken from the RRUFF database [28]. SEM imaging and analyses were performed with a Gemini 500 (Zeiss) with 15 kV acceleration voltage and equipped with a Quantax Energy Dispersive X-ray Spectroscopy (EDS) microanalysis system (Bruker). Samples were prepared following two procedures: in one procedure, the sample powder was dispersed on the sample holder covered by a conductive carbon tape and then the assembly was metallized with gold coating; in a second procedure, the powder was embedded close to the surface of an epoxy stab and then polished. The first procedure was utilized to observe the pristine powder morphology, whereas the second one was utilized to investigate the core composition and morphology of the crystallites in the products.

3. Results

3.1. Kinetics of CO_2 capture

Fig. 1a reports the pressure inside the reaction vessel as a function of time, measured during the carbonation treatments.

As can be observed, the pressure initially decreases due to the combined effect of CO_2 dissolution in water and carbonation of brucite. However, pressure decrease due to CO_2 dissolution can be detected for treatments at setpoint $T = 40\,°C$, but it is not detected already at $T = 70\,°C$ (see Figs. S2 and S3 showing the treatments performed on blank samples). In order to evaluate the effect of CO_2 absorption by pure water (reaction 1), we can estimate from Fig. S2 a pressure decrease of about 1.0 bar occurring within the first 10 min. At 40 °C, this corresponds to the transfer of 0.023 mol of CO_2 for the gas into the liquid phase (volume: 300 ml), determining a solubility of 1.4×10^{-3} molar fraction (3.4 g l^{-1}) at about 1 MPa, which well compares with data reported in the literature [29]. In any case, pressure decrease is contrasted by the pressure increment due to the progressive heating of the slurry. As a result, pressure loses a monotonic decreasing trend for setpoint temperatures higher than 100 °C. Within the range 100–145 °C, pressure reaches a maximum value at $t = 600\,s$, whereas, for $T > 145\,°C$, pressure reaches the maximum some minutes after the onset of the dwelling stage, probably due to delayed thermalization of the whole reaction vessel (liquid and vapor phase).

A pressure decrease recorded during the dwelling stage is indicative of the progress of the carbonation reaction. For this reason, we can consider the first derivative with changed sign of the pressure curves reported in Fig. 1a as a parameter proportional to the reaction rate. Fig. 2 reports the derivative curves obtained from Fig. 1a, displayed in three temperature intervals for a better visualization.

For the first three curves at low temperature (23, 40, and 55 °C), the reaction progress appears to be independent on temperature, showing a decreasing rate intersecting the abscissa at about 80 min. This duration can then be considered as the time needed to saturate the CO_2 capturing capability of the system. At 70 °C, the reaction rate is still monotonically decreasing, however, saturation is reached after about 45 min. From 85 to 145 °C, the reaction rate reaches a maximum at the onset of the dwelling stage, and the CO_2 capture saturates at progressively shorter times, from 40 to 15 min. At temperatures higher than 145 °C, the graph in Fig. 2 shows curves having no point in the first Cartesian quadrant, indicating that CO_2 capture saturates within the 10 min-time interval of
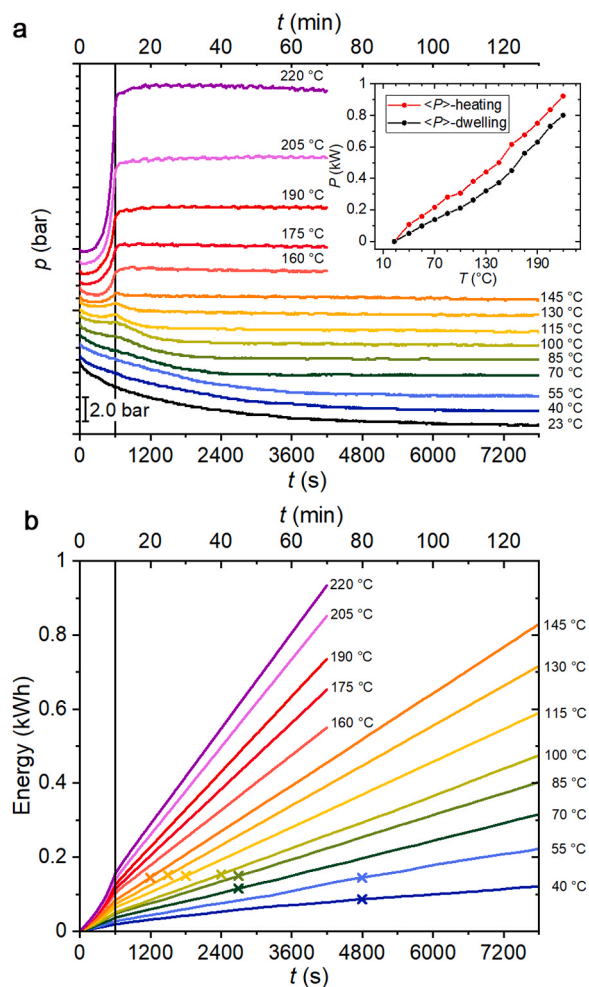

Fig. 1. (a) Reactor pressure monitored during carbonation reaction of brucite at various temperatures, from 23 to 220 °C. Starting pressure was 12 bar (6 bar CO_2 + 6 bar N_2, curves are vertically shifted for clarity). The bottommost curve corresponds to a treatment with no MW (at RT: 23 °C). For subsequent curves, from 0 to 600 s (*heating* stage) the temperature was incremented at a constant rate through MW irradiation to reach the setpoint temperature (*dwelling* stage, highlighted by the vertical solid line at $t = 600\,s$). Setpoint temperature was 40 °C for the second curve starting from the bottom and was augmented by 15 °C for the next ones, up to 220 °C. The inset reports the average MW power ($<P>$) supplied during the heating and dwelling stages of the setpoint temperatures explored. (b) MW energy (integrated power) delivered in the reactor during the heating treatments at various temperatures. Crosses identify the times at which pressure stabilizes, indicating termination of CO_2 capture.

the heating stage.

In the inset of Fig. 1a, one can see the average MW power supplied by the synthesizer during the reaction runs. The time integral of power data provides the MW energy supplied by the system during the treatments; these energies are displayed in Fig. 1b. The crosses superimposed on the energy curves identify the time at which the CO_2 uptake is complete on the bases of the data in Fig. 2. Table 1 summarizes the MW energy and time required to saturate the CO_2 capture for each of the setpoint temperatures explored.

It is interesting to note that, as shown by the last column of Table 1, for temperatures higher than 40 °C, the energy needed to complete CO_2 capture is rather independent on the setpoint temperature and settles to about 0.15 kWh.

To get deeper insights into the CO_2 capture process assisted by MW, we performed similar treatments on equinormal solutions of sodium hydroxide (0.2 mol NaOH in 300 ml of deionized water). In the treatments of NaOH solution with CO_2, reactions (2) and (3) are substituted
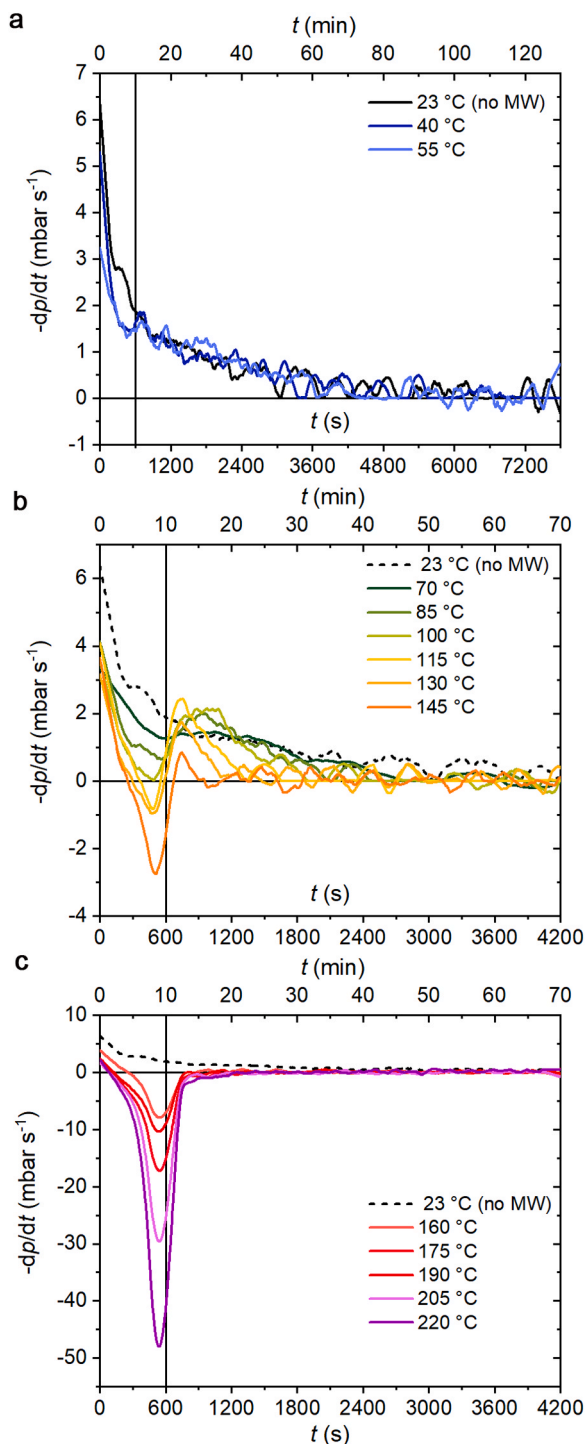
Fig. 2. First derivative with changed sign of the pressure curves reported in Fig. 1a for the carbonation experiments executed at a setpoint temperature of 23 (with no MW radiation), 40 and 55 °C (a), for those executed at setpoint temperatures from 70 to 145 °C (b), and for those executed at setpoint temperatures from 160 to 220 °C (c).

by the following reaction:

$$2Na^+_{aq} + 2OH^-_{aq} + H_2CO_{3,aq} = 2Na^+_{aq} + CO^{2-}_{3,aq} + 2H_2O \quad (4)$$
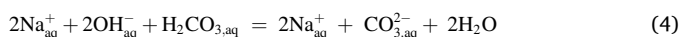
Reaction (4), *i.e.*, the neutralization of carbonic acid by a strong base, and reaction (3), *i.e.*, the precipitation of Mg-carbonates, are rapid processes and probably enhanced by MW. Therefore, in the carbonation of NaOH solutions, the rate-limiting process is represented by the gas to

Table 1
MW energy and time spent for CO_2 capture saturation.

Setpoint T	E-heating stage	E-dwelling stage	Total E
°C	kWh (duration)	kWh (duration)	kWh
23	0	0 (80 min)	0
40	0.018 (10 min)	0.060 (70 min)	0.078
55	0.027 (10 min)	0.11 (70 min)	0.14
70	0.036 (10 min)	0.081 (35 min)	0.12
85	0.047 (10 min)	0.10 (35 min)	0.15
100	0.051 (10 min)	0.11 (30 min)	0.16
115	0.063 (10 min)	0.088 (20 min)	0.15
130	0.074 (10 min)	0.078 (15 min)	0.15
145	0.084 (10 min)	0.066 (10 min)	0.15
160	0.10 (<10 min)	0.0 (0 min)	< 0.10
175	0.11 (<10 min)	0.0 (0 min)	< 0.11
190	0.13 (<10 min)	0.0 (0 min)	< 0.13
205	0.14 (<10 min)	0.0 (0 min)	< 0.14
220	0.15 (<10 min)	0.0 (0 min)	< 0.15

liquid transfer of CO_2 [see reaction (1)], and the monitoring of CO_2 capture in this system allows us to get an estimate of the rate of this transfer process and to evaluate the impact on the carbonation rate of reactions (2) and (3), *i.e.*, the acid solubilization and neutralization of brucite and the possible passivation effect induced by the precipitation of carbonates.

In Fig. 3, one can see the comparison of the pressure trend recorded in treatments performed at three representative temperatures of 40, 70 and 100 °C on brucite slurries and NaOH solutions.

At 40 °C (and 55 °C, not reported) and intermediate times, one can observe a slight deviation of the two curves, with that corresponding to brucite slurries having, as expected, a lower decreasing rate. At late times, the two curves reconnect and reach a plateau at the same pressure level, indicating that the stoichiometry of CO_2 capture in the two processes is the same. For higher temperatures, the deviation between the two curves is more pronounced and increases with time. Finally, at late times, the two curves do not reconnect, but saturate at different pressure levels. This difference is 1.4 bar at 70 °C, and 1.6 bar at 100 °C. These pressure differences both correspond to 0.03 mol of gas at the corresponding temperatures, as can be estimated by the equation of state of an ideal gas. This behaviour is maintained in treatments at setpoint
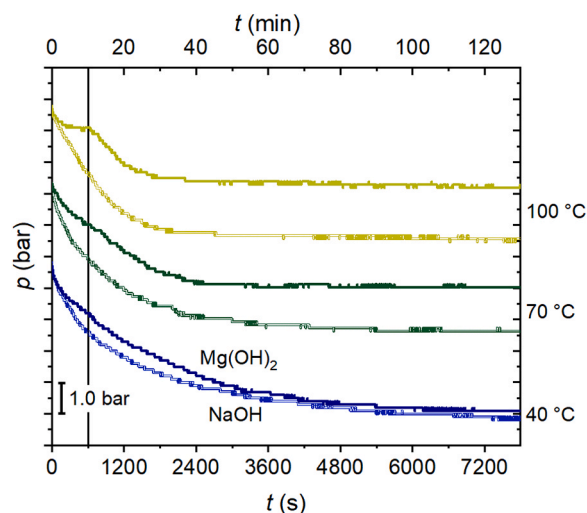

Fig. 3. Reactor pressure monitored during carbonation reaction of brucite and equinormal solutions of NaOH at 40, 70, and 100 °C. Starting pressure was 12 bar (6 bar CO_2 + 6 bar N_2, curves are vertically shifted for clarity). From 0 to 600 s (*heating* stage) the temperature was incremented at a constant rate through MW irradiation to reach the setpoint temperature (*dwelling* stage, highlighted by the vertical solid line at $t = 600$ s). The energy required during the treatments of the two solutions are displayed in Fig. S4. Pressure differences at end treatment are 1.4 bar and 1.6 bar at 70 and 100 °C, respectively.

temperature up to 205 °C. This result demonstrates that the stoichiometry of CO_2 capture changes between 55 and 70 °C.

3.2. Analysis of the reaction products: precipitates

At the end of the carbonation treatments, the reactor content appeared very similar to the initial slurry, with a remnant effervescence due to the excess of CO_2. After centrifugation and separation of the precipitate and supernatant liquid, the former was subjected to PXRD, SEM and Raman spectroscopy analyses to identify mineral phases.

Fig. 4 displays the results of PXRD carried out on the precipitates obtained. For temperatures in the range 23–55 °C, the sole identifiable crystal phase was monoclinic nesquehonite [30] (see also Fig. S5), with a trace amount of hexagonal brucite (Fig. 8 and S1) [31]. From 70 to 190 °C, the unique crystal phase of the precipitate was identified as monoclinic hydromagnesite [32] (Fig. S6). At 205 °C, the precipitate presents a detectable trace amount of hexagonal magnesite [33] (Fig. S7), which becomes the dominant crystal phase at 220 °C, in coexistence with hydromagnesite and brucite, with phase contents of 62.2(2), 33.1(2), and 4.6(1) wt%, as evaluated from a quantitative PXRD analysis, and using standard references by [33], [32] and [31], respectively.

The patterns shown in the lower panel of Fig. 4b allow us to notice a progressive increase in crystallinity of the hydromagnesite product, proven by the decreasing width and increasing intensity of the low angle diffraction peaks. A progressive shift of the lowest angle peak [(100) reflection in Fig. S6] is also detectable, being centered at $2\theta = 9.15°$ at 70 °C, and reaching the expected position at $2\theta = 9.61°$ only at $T \geq 130$ °C. This shift is consistent with a structure expanded by 5% along a^*. The analysis of crystallinity evolution was performed by applying the Scherrer equation to the most intense peaks in the diffraction patterns of Fig. 4. The crystallite size perpendicular to the (hkl) plane, D_{hkl}, is obtained as: $D_{hkl} = K\lambda/\beta_{hkl}\cos\theta$; where θ is the Bragg angle, β_{hkl} is the full width at half maximum of the hkl diffraction peak, and K is a crystallite-shape dependent parameter set to 0.9. The results of the Scherrer analysis are reported in Fig. 5b, together with SEM images acquired on the obtained products dispersed on carbon tape. Note that dihedral angles of the indicated planes are: $(101)\widehat{\ }(200) = 32.30°$, $(100)\widehat{\ }(011) = 71.64°$, $(104)\widehat{\ }(2\bar{1}3) = 32.47°$, indicating that the size is evaluated along two substantially different direction across the crystallites.

The SEM images in Fig. 5a,d-f allow to establish that flakes are the dominant morphological motif of the identified carbonate crystallites in the temperature range 40–200 °C. Flake-like crystallites are ill-defined at $T < 70$ °C (Fig. 5a,d); moreover, at $T = 40$ °C, rod-like crystallites are sometimes identifiable within a layer of flake-like crystallites (Fig. 5d). Carbonate flakes get well-shaped at $T > 70$ °C and organized in spherulites (Fig. 5e,f). At $T > 200$ °C, rhombohedral crystallites appear, coexisting with flake-like domains (Fig. 5c).

The identification of the aforementioned dominant crystal phases corresponds both to products obtained after the treatment times reported in Fig. 1a and after the CO_2 capture saturation times indicated by the crosses in Fig. 1b and reported in Table 1. This evidence allows us to conclude that CO_2 capture saturation corresponds to completion of the carbonation reaction, in accordance with the assumption that the precipitation of the carbonate phase (reaction 3) is not the rate-limiting step of the process. The disclosed chemical nature of the products allows us to determine the mass yield achieved in each reaction run, in accordance with the following equations:
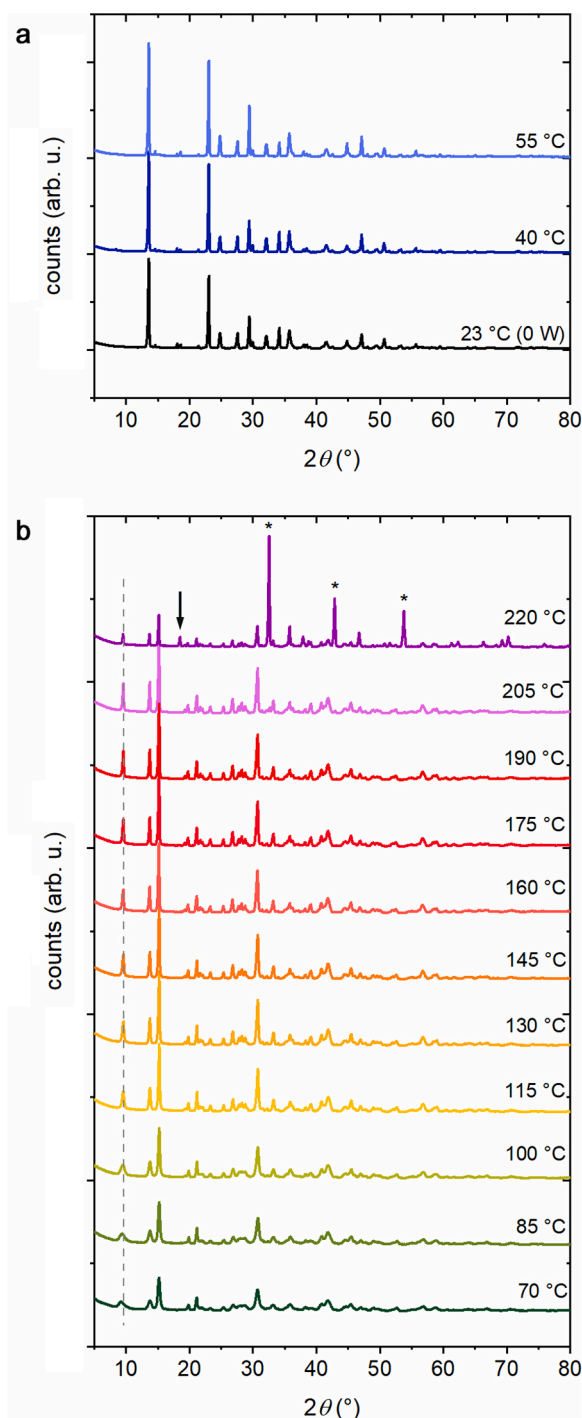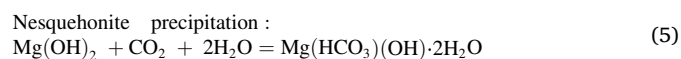
Nesquehonite precipitation :
$$Mg(OH)_2 + CO_2 + 2H_2O = Mg(HCO_3)(OH)\cdot 2H_2O \qquad (5)$$

Fig. 4. PXRD patterns obtained on the precipitated products of the carbonation reactions of brucite performed at the setpoint temperature indicated on the right of each curve. (a) At temperature between 23 and 55 °C, the patterns correspond to a dominant phase of nesquehonite. (b) At temperature between 70 and 205 °C, the patterns correspond to a dominant phase of hydromagnesite, with crystallinity increasing with temperature; the vertical dashed line highlights the low-temperature shift of the (100) reflection of hydromagnesite. At temperature 220 °C, the pattern corresponds to a mixture of magnesite [(104), (2−1 3), (1 0−8) reflections marked by *], hydromagnesite, and brucite [(001) reflection marked by the arrow].
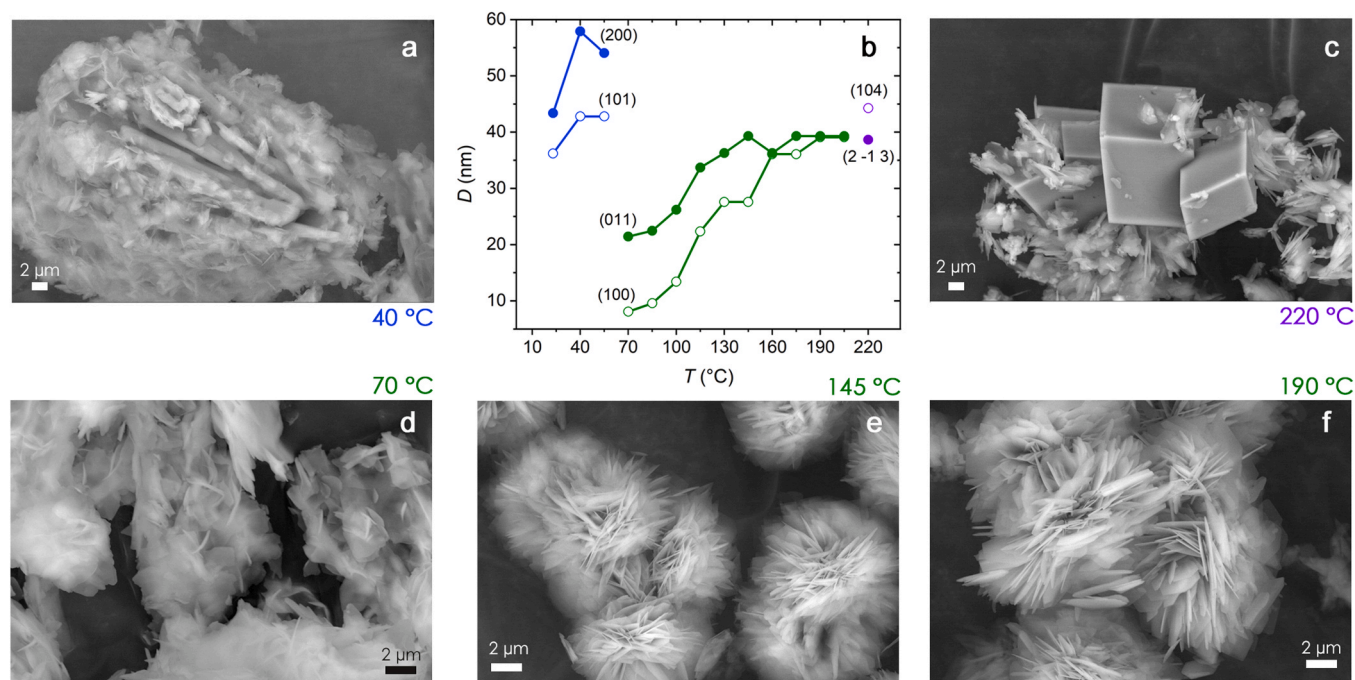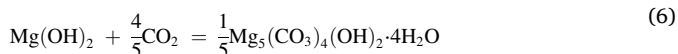
Fig. 5. (a, c-f) SEM images acquired on precipitate powders obtained at the temperatures indicated are arranged in panels around the graph. (b) Crystal domain size as a function of temperature as deduced by the Scherrer equation applied to diffraction peaks indicated in parenthesis (blue: nesquehonite, green: hydromagnesite, violet: magnesite). See Figs. S5-S7 for peak indexation.

Hydromagnesite precipitation:

$$Mg(OH)_2 + \frac{4}{5}CO_2 = \frac{1}{5}Mg_5(CO_3)_4(OH)_2 \cdot 4H_2O \tag{6}$$

Magnesite precipitation:
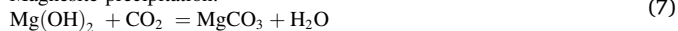$$Mg(OH)_2 + CO_2 = MgCO_3 + H_2O \tag{7}$$

Table 2 reports the initial brucite mass, the product mass, and the yield of each carbonation run.

It is apparent that, in the temperature range of formation of nesquehonite, the yield is very low, settling around 40–50%, whereas it is about 80–90% in the temperature range of formation of hydromagnesite. The yield of 81% obtained for 220 °C represents an estimate performed on the basis of the characterized mixture composed by 62.2 (2) wt% of magnesite, 33.1(2) wt% of hydromagnesite, and 4.6(1) wt% of brucite. Moreover, a slight increase of yield with temperature is observable.

We point out that, even for setpoint temperatures higher than

220 °C, precipitates are formed by a mixture of magnesite and hydromagnesite. To investigate the presence of possible composite structures of precipitate particles [*i.e.*, (i) the formation of a nesquehonite core, nucleating during the heating stage, surrounded by a layer of hydromagnesite or (ii) the formation of a hydromagnesite core, nucleating during the heating stage, surrounded by a layer of magnesite], we compared the SEM morphology of polished sections of the precipitates embedded in epoxy with that one of precipitates dispersed on carbon tapes. The results are reported in Fig. 6.

Only the precipitate of the sample reacted at 40 °C shows a change in morphology as a consequence of sectioning. Indeed, the characteristic needle-like morphology of nesquehonite [34] is evident only in the polished embedded sample, while the pristine powder shows aggregates with a surface decorated by flake-like crystallites, which are typical of hydromagnesite [35]. Finally, rhombohedral crystallites are attributed to magnesite (Fig. 5c and Fig. 6c,f) [36].

Fig. 7 shows the Raman spectra of the different samples of brucite subjected to carbonation. Two spectral ranges provide most of the information about the sample composition and structure, namely the 1040–1180 cm^{-1} range, where the symmetric CO_3^{2-} stretching is present, and the 3000–3800 cm^{-1} range, where the OH stretching vibrations are found.

As shown in the bottom part of Fig. 7, brucite samples before carbonation present the sharp OH stretching signal at about 3650 cm^{-1} (Fig. 7b) [37] and do not show any signal of carbonate groups, as indeed evidenced by the absence of the symmetric CO_3^{2-} stretching Raman signal (Fig. 7a). At 23 °C, *i.e.*, in absence of MW radiation, brucite transforms into nesquehonite, which is proved by the observation of the symmetric CO_3^{2-} stretching Raman signal at 1100 cm^{-1} (Fig. 7a), and the broad and characteristic structure of the Raman signals in the OH stretching region, which is due to the expected presence of water molecules in the crystal structure (Fig. 7b) [38]. Notably, the peak at about 3650 cm^{-1} overlaps with both the brucite isolated OH stretching and one of the two OH stretching features of hydromagnesite. We deduce that the reaction to nesquehonite might be not complete, with the precipitate phase presenting some brucite residues and possibly a small fraction of
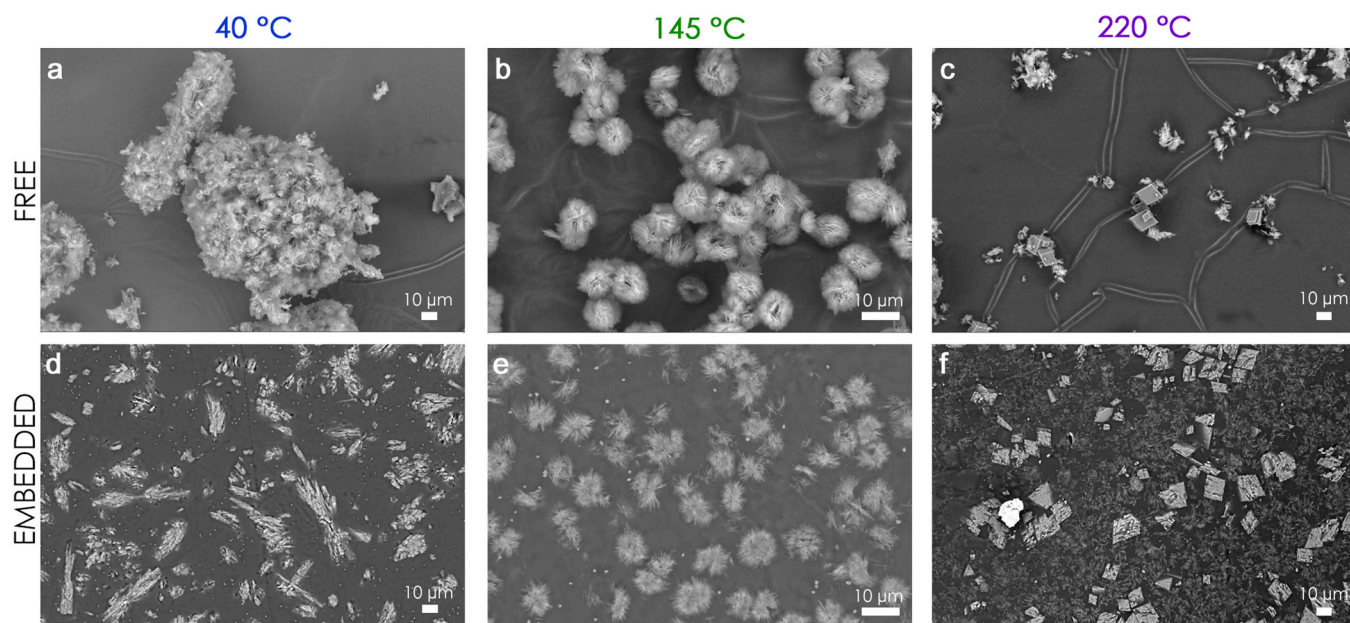
Table 2

Mass yield of precipitates obtained at the end of the carbonation reactions. Prevalent products are: nesquehonite (23–55 °C), hydromagnesite (70–205 °C), and magnesite (220 °C).

Setpoint T	Brucite mass	Precipitate mass	Yield
°C	g	g	%
23 (no MW)	5.51	5.51	42
40	5.51	5.95	46
55	5.54	6.91	53
70	5.53	6.75	76
85	5.51	6.77	77
100	5.53	7.36	83
115	5.53	7.26	82
130	5.52	7.64	87
145	5.51	7.55	86
160	5.43	7.58	87
175	5.50	7.92	90
190	5.52	8.11	92
205	5.44	8.00	92
220	5.51	7.75	81

Fig. 6. SEM images of reaction precipitates obtained at 40, 145, and 220 °C, as free powders deposited on conductive carbon tape (a-c), and sectioned and polished powders embedded in araldite (d-f).
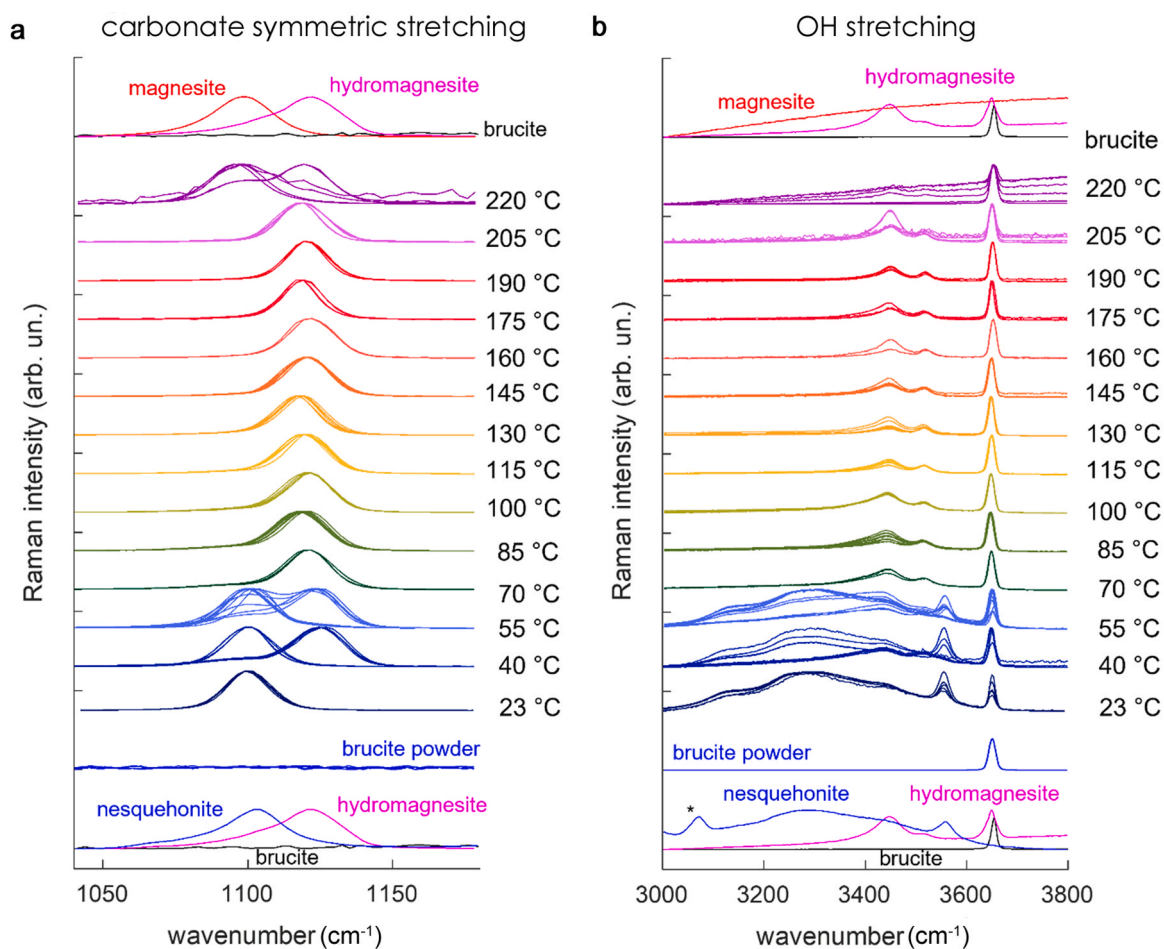

Fig. 7. Raman spectra of the samples of carbonated brucite for the different setpoint temperatures reached during the carbonation reaction. Spatial variability of the carbonate phases is significant only for the temperatures of 40, 55, and 220 °C. For these samples, the number of collected Raman spectra (see Section 2, "Materials and Methods") is enough to fully characterize them. The reference spectra of brucite, hydromagnesite, magnesite, and nesquehonite are placed for the sake of comparison at the top and bottom parts of each panel. The peak marked with a star is assigned to a possible contaminant, as proved by comparison with another Raman spectrum of synthetic nesquehonite reported in the literature, where this peak is absent [40].

hydromagnesite.

At higher temperatures (40 and 55 °C) we observe (both in the CO_3^{2-} stretching region, Fig. 7a, and the OH stretching region, Fig. 7b) a progressive increase of hydromagnesite content. The sample composition becomes then mainly hydromagnesite at temperatures located between 70 °C and 205 °C, as indicated by the symmetric CO_3^{2-} stretching Raman signal at 1122 cm^{-1} and by the three OH stretching bands at 3444, 3516 and 3650 cm^{-1} [39]. Finally, at 220 °C, in accordance with the results of PXRD, we observe the co-presence of hydromagnesite and magnesite; in fact, the increasing slope at higher wavenumbers, visible in Fig. 7b, is caused by the presence of magnesite, as evident from the comparison with the reference spectrum.

3.3. Analysis of the reaction products: solid residue of supernatant solutions

As shown in Table 2, the relatively low yield of nesquehonite precipitates indicates that a significant fraction of products is in solution. PXRD patterns of the solid residue of exsiccated supernatant solutions obtained in treatments in the temperature range 23–55 °C and 70–205 °C are reported in Fig. 8 and Fig. 9, respectively. In Fig. 8, the comparison with the diffraction pattern of the related precipitate phase demonstrates that the exsiccated solution is composed by nesquehonite, with a higher crystallinity and devoid of detectable amounts of brucite.

In Fig. 9, the exsiccated solution has a composition that depends on the exsiccation temperature: for a temperature as low as 50 °C, the crystallized phase is attributable to dypingite [$Mg_5(CO_3)_4(OH)_2 \cdot 5H_2O$] [41]. For higher temperatures, the crystallized phase is a mixture of dypingite and hydromagnesite, which becomes the dominant phase at 110 °C.

We note that, at high crystallization temperature, a third phase is detected, characterized by a diffraction peak at 7.46°, corresponding to an interlayer spacing of 11.8 Å. This reflection cannot be attributed to known phases of MHCH.

Finally, the supernatant solution of reactions undertaken at 220 °C crystallizes as hydromagnesite, while maintaining the trace of the undetermined phase with spacing of 11.8 Å (Fig. 10).

The statistical analysis of the Raman spectra, performed in different points of the exsiccated solutions, provides support to the interpretation
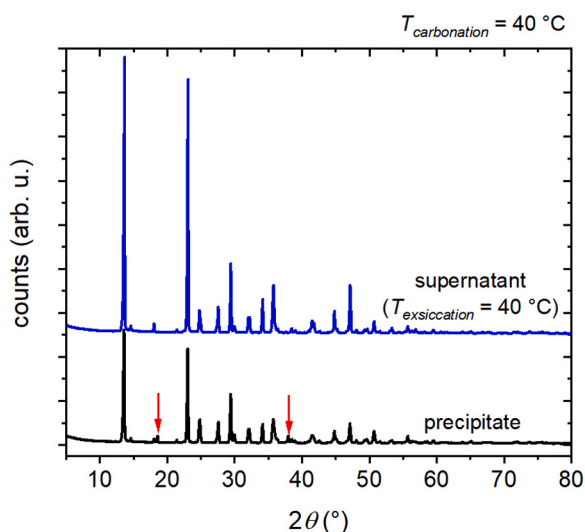

Fig. 9. Comparison between PXRD patterns obtained on the precipitated product and on the solid residue of the exsiccated supernatant solution of the carbonation reactions performed at a setpoint temperature of 145 °C. The precipitate pattern corresponds to a pure hydromagnesite phase. By changing the exsiccation temperature of the supernatant solution, the detected crystal phase change from dypingite (blue pattern), a mixture of dypingite/hydromagnesite (green pattern), and hydromagnesite (red pattern). The blue arrow indicates a reflection at 7.46° (*d-spacing*: 11.8 Å) which is recurrent in exsiccated supernatant solutions obtained at setpoint temperature higher than 70 °C.
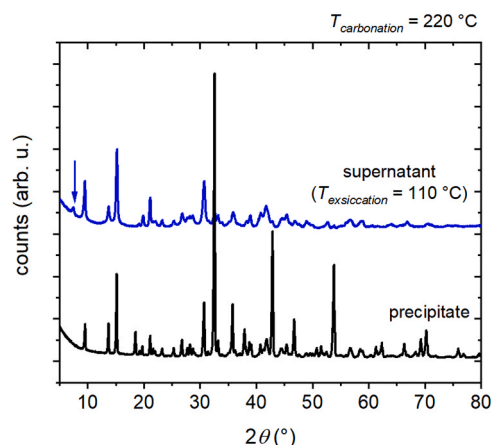
Fig. 10. Comparison between PXRD patterns obtained on the precipitated product and the exsiccated supernatant solution of the carbonation reactions performed at a setpoint temperature of 220 °C. The precipitate pattern corresponds to a mixed phase of magnesite and hydromagnesite. The supernatant pattern corresponds to a phase of hydromagnesite. The blue arrow indicates the presence of the undetermined phase with spacing 11.8 Å.

of the PXRD results (Fig. S8). Indeed, spectra show that the supernatant from the reaction at 40 °C corresponds to nesquehonite, as clearly indicated by the carbonate symmetric stretching at 1100 cm^{-1} (Fig. S8a) and the structured OH stretching band extending between 3000 and 3600 cm^{-1} (Fig. S8b). The supernatant residue from the reaction at 145 °C corresponds mainly to hydromagnesite, as indicated by the carbonate symmetric stretching at 1122 cm^{-1}, and the characteristic three bands in the OH stretching region. Finally, also the supernatant sample from the reaction at 220 °C corresponds to hydromagnesite.

The SEM images acquired on solid residues of supernatant solutions obtained at 40 °C show the clear presence of rod-like nesquehonite crystallites, reaching sizes of hundreds of micrometres (Fig. S9), explaining the substantial increment of the signal reported in the PXRD

Fig. 8. Comparison between PXRD patterns obtained on the precipitated product and on the solid residue of the exsiccated supernatant solution of the carbonation reactions performed at a setpoint temperature of 40 °C. The precipitate pattern corresponds to a phase of nesquehonite containing a slight brucite residue [red arrows indicate the (001) and (101) reflections of brucite]. The supernatant pattern corresponds to a pure phase of nesquehonite.
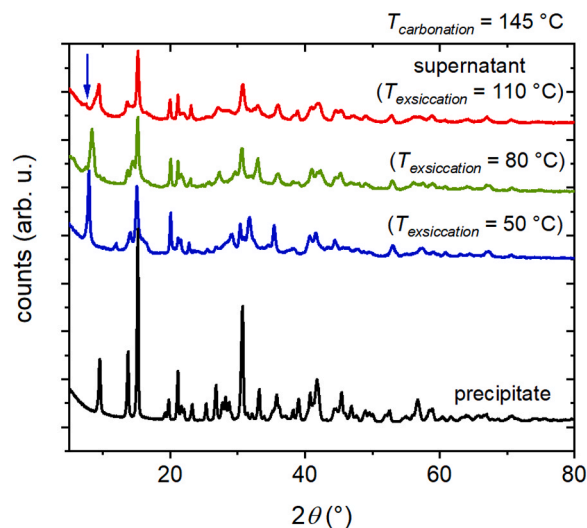
pattern of Fig. 8. The solid residues obtained at higher carbonation temperatures are composed by flake-like and fibrous aggregates, consistently with possible mixtures of hydromagnesite and dypingite.

4. Discussion

From RT (23 °C) up to 55 °C, the dominant product of MW-driven carbonation of brucite was identified as nesquehonite. A nesquehonite precipitate, having XRD detectable traces of residual brucite, is obtained with a yield as low as 50% (Table 2). This result is due to the relatively high solubility of nesquehonite in water, enhanced by the excess of CO_2 [42]. The kinetics curves (Fig. 2), and the results of the PXRD analysis (Fig. 4), do not allow to highlight substantial differences in the dynamics and the product characteristics obtained within this range of temperature. However, the higher sensitivity of Raman spectroscopy reveals a useful feature which allows for the identification of a characteristic effect pertaining to the use of MW radiation. Indeed, as can be observed in Fig. 7, superimposed hydromagnesite and nesquehonite signals are evident already in precipitates obtained by MW heating at 40 °C, but are absent in the precipitate obtained without MW irradiation at RT. This indicates that MW radiation triggers the phase transition to hydromagnesite [43,44]. In accordance with this evidence, the solid residue of supernatant solutions obtained in treatments performed at 40 and 55 °C and dried at 40 °C do not show any vibrational signal attributable to hydromagnesite (Fig. S8). The direct precipitation of hydromagnesite as a product of carbonation of brucite occurs at temperature higher than 70 °C, as evidenced both in PXRD and Raman spectra (Figs. 4 and 7). However, before reaching the setpoint temperature, the previously formed nesquehonite undergoes a phase transformation, as evidenced by the pseudomorphic rod-like habit of the hydromagnesite crystallites [45] obtained at 70 °C and displayed in Fig. 11.

The evidence of the occurrence of a phase transformation is reflected by the compared pressure trends reported in Fig. 3 and the PXRD patterns in Fig. 4 for the temperature range of 70–145 °C. Indeed, the late-time coincidence of the pressure curves collected at 40 °C (Fig. 3) indicates the progression of two reactions with the same stoichiometry of CO_2 capture, in accordance with reactions (4) and (5). On the contrary, the separation of the pressure curves collected at 70 and 100 °C (Fig. 3) can be attributed to the pressure increment due to the release of CO_2 and water consequent to the nesquehonite-to-hydromagnesite transition:

$$Mg(HCO_3)(OH)\cdot 2H_2O = \frac{1}{5}Mg_5(CO_3)_4(OH)_2\cdot 4H_2O + \frac{1}{5}CO_2 + 2H_2O$$

(8)
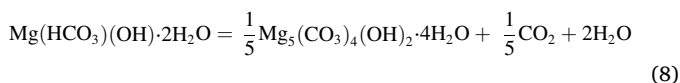
The stoichiometric ratio of 1/5 between the released CO_2 and the Mg-carbonate accounts exactly for the 0.03 mol increment responsible for the pressure increase observed at late times in the collected curves in Fig. 3. Moreover, the hydromagnesite phase precipitated at these temperatures display a substantial expansion of the (100) planes, reaching a maximum of *ca.* 5% at 70 °C, as a consequence of the transformation from a low-density phase (nesquehonite: 1.85 g cm⁻³) to a high-density one (hydromagnesite: 2.25 g cm⁻³). As recently discussed [46], the

nesquehonite surface can be considered as a precursor for the nucleation and seeding of both hydromagnesite and dypingite, promoting the formation of the texture called "house of cards", the result of a dissolution-recrystallization self-assembly growth mechanism. When the dissolution rate of nesquehonite is faster than the precipitation rate of hydromagnesite, and nesquehonite is the dominating phase of MHCH, the surface of nesquehonite rod-like crystals is transformed into hydromagnesite; however, high values of CO_2 concentration, pH, and $Mg(OH)_2/CO_2$ molar ratio may involve the formation of rosette-like dypingite flakes [46]. In our study, considering the experimental conditions chosen, and the resulting observations, the attribution to hydromagnesite, rather than dypingite, of the flakes formed on nesquehonite rods appears to be properly motivated.

Once the temperature range of the direct nucleation of hydromagnesite is reached, mass yield increases to a great extent as a consequence of the reduced solubility of this phase (Table 2) [47]. In the temperature range 70–205 °C, the increment of the setpoint temperature gives rise to a progressive reduction of the initial mass fraction of nucleated nesquehonite, as evidenced by the increasing separation with temperature during the heating stage of the curves in Fig. 3, and a progressive increment of the overall reaction rate. Contemporarily, the nucleated products display a progressive increment of crystallinity in terms of size of coherent domains and development of a spherulitic morphology (Fig. 5). It must be noted that this result is not accomplished by a prolonged thermal heating after reaction completion, rather by a relatively rapid process (within few minutes at $T > 145$ °C, as shown in Fig. 2) driven by the use of MW radiation. Recent studies show that, by conventional thermal heating, the product of water-mediated brucite carbonation can be varied in accordance with our results, passing from nesquehonite at low temperature (< 50 °C) [15], to hydromagnesite at intermediate temperatures (150 °C), and to magnesite at high temperature (> 200 °C) [16]. In these studies, CO_2 partial pressure is maintained constantly as high as 15 bar. The reaction kinetics is inferred *ex situ* by the measurement over time of the fraction of carbonate phase in the precipitated solid and the concentration of ionic species in the liquid phase. At 30 °C, the time for carbonation completion is reported to be 80 min [16], which coincides with our results in the range 23–55 °C (Table 1). It is worth underlying that, despite the more favourable conditions adopted in these studies (*i.e.*, the use of 15 bar of pure CO_2), reaction times for carbonation completion at higher temperatures are substantially longer than those required in our experiments. At 150 °C and 200 °C reaction time is reported to be 60 min and 45 min, respectively [16], whereas we recorded a reaction time of 20 min at 145 °C, and it set below 10 min for higher temperatures. As a final remark, we evidenced an increase in the yield with temperature of the precipitated phase (Table 2), which is in contrast to that expected on the basis of the temperature dependence of the solubility of the products. This can be attributed to the use of MW since, even though the radiative energy spent for the treatments is independent on the setpoint temperature (Fig. 1b and Table 1), the MW intensity increases with temperature (inset of Fig. 1a), favouring the process of crystallization [23].

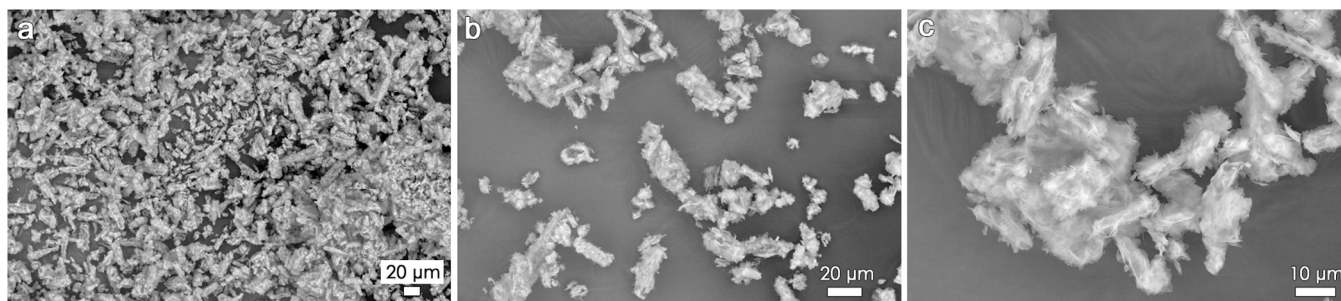The formation of rhombic crystallites of magnesite, as those shown in

Fig. 11. SEM micrographs acquired on the solid precipitate obtained in carbonation experiment at 70 °C.

Figs. 5c and 6c, occurs at temperature as low as 190 °C, even though neither the PXRD nor Raman spectra analyses reveal their presence, and magnesite becomes the dominant phase at $T > 220$ °C. Contrary to nesquehonite, hydromagnesite is not involved in a solid-solid transition to magnesite, as evidenced by the isolated character of rhombic crystallites of magnesite and their compact structure (Fig. 6). However, the presence of a brucite residue in the products obtained at 220 °C indicates a possible mechanism of passivation of brucite by heterogeneous nucleation of magnesite and embedding. On the contrary, the absence of a significant amount of brucite residue in the products obtained at any other temperature indicates that this mechanism is not active neither for nesquehonite nucleation nor for hydromagnesite nucleation.

As far as dried supernatant solutions are concerned, it is interesting to note that the solid residues maintain a "memory" of the precipitate phase, possibly due to some colloidal particles that remain suspended in the supernatant even after separation which induce the subsequent crystallization. Indeed, by drying the supernatant solutions obtained at $T < 70$ °C, the solid residue is composed by a very pure and crystalline nesquehonite phase (Fig. 8). Dried supernatant solutions obtained from carbonation experiments performed at $T \geq 70$ °C contain hydromagnesite as a dominant phase (Figs. 9, 10, and S8). However, depending on the drying conditions (*i.e.*, temperature and time), the level of hydration of the MHCH phases might vary, bringing about the formation of dypingite, which contains one mole per unit formula of additional water with respect to hydromagnesite, to possibly other phases with higher levels of hydration, such that the one we observe with an interlayer spacing of 11.8 Å (Figs. 9 and 10). As recently discussed [48,49], dypingite should be considered as a series of phases with different hydration degrees, instead of an unique one. Its peculiar characteristics, such as the position of diffraction peaks at *ca.* 8.5°, 16°, and 31°, are dependent on the amount of water molecules, which is a parameter controlled by the ambient humidity. Moreover, the hydration level is strictly related with the carbonation reaction evolution, since an amorphous precursor might be converted into a structurally semi-ordered phase (*i.e.*, dypingite), which slowly becomes more organized, following the Ostwald step rule, according to which the phase transformation promotes a structurally similar phase, rather than a thermodynamically more stable one [45].

5. Conclusions

This work illustrates the application of MW chemistry to drive and monitor the carbonation reaction of water-based brucite slurries into MHCH. MW irradiation, along with the setup adopted, allowed for the achievement of the fine control on temperature and pressure of the reactor and the minimization of the energy spent for the heating of the heterogeneous mixture of reactants. We identified a temperature range of 23–55 °C in which nesquehonite represents the dominant phase obtained as precipitate and as dried supernatant. Within the same range, we verified that MW irradiation triggers the transition of the surface of nesquehonite crystallites into hydromagnesite. This latter phase represents the dominant phase obtained in precipitates and dried supernatant solutions processed within the temperature range of 70–205 °C. MW irradiation allows for a quantitative transformation of reactants within times shorter than 10 min, being substantially shorter than those reported for carbonation carried out under conventional convective heating conditions. This reaction rate increment is accomplished thanks to the MW-induced acceleration of both the acid dissolution step of brucite and the precipitation step of Mg-carbonates. Temperature increase was demonstrated to promote a progressive increment of the crystallinity of the hydromagnesite products. The increment of average MW intensity with temperature stimulates the crystallization process, allowing for the raise of the yield in terms of fraction of precipitated phase. Finally, magnesite was observed to start nucleating at temperature as low as 190 °C, becoming the dominant phase for $T \geq 220$ °C. However, the hydromagnesite produced during the heating stage of the

treatments does not undergo a transition into magnesite, preventing the possibility to obtain a pure magnesite phase even at higher temperature.

The advantages associated with the use of MW radiation rely primarily on the possibility to transfer heat efficiently and uniformly within the volume of the reactant mass and to enhance the diffusion coefficient of electrolytes. Furthermore, specific processes having non-thermal origin can be exploited for incrementing the reaction rate. Within the framework of the carbonation reaction, a potentially valuable non-thermal process is represented by the de-solvation effect of ions in MW field predicted by molecular dynamics simulations [50]. In particular, Mg^{2+} ions, which are known to bind effectively water [51], might undergo de-solvation as a consequence of the interaction with MW. This effect would in principle favour the precipitation of magnesite and contrast the precipitation of the MHCH usually observed [52–54]. Under the MW irradiation intensity adopted in this work, there is no evidence of the occurrence of such de-solvation process, allowing for the precipitation of magnesite at low temperature. This motivates to test in future experiments if the required intensity of the MW field intensity for de-solvation can be achieved experimentally.

Supplementary data

SEM and PXRD analysis of pristine brucite, *T-p* curves collected on MW treatments performed on blank samples, PXRD pattern indexation, Raman spectroscopy of dried supernatants, SEM analysis of dried supernatants.

CRediT authorship contribution statement

Capitani Giancarlo: Data curation, Methodology. **Lucotti Andrea:** Data curation, Investigation, Methodology, Writing – original draft. **Yivlialin Rossella:** Data curation, Investigation, Validation. **Tommasini Matteo:** Investigation, Methodology, Resources, Writing – original draft. **Campione Marcello:** Conceptualization, Formal analysis, Investigation, Methodology, Supervision, Writing – original draft, Writing – review & editing. **Corti Mattia:** Investigation, Methodology. **D'Alessio Daniela:** Methodology, Investigation, Formal analysis, Writing. **Bussetti Gianlorenzo:** Project administration, Resources. **Malaspina Nadia:** Funding acquisition, Project administration, Resources.

Declaration of Competing Interest

The authors declare that they have no known competing financial interests or personal relationships that could have appeared to influence the work reported in this paper.

Data Availability

Data will be made available on request.

Appendix A. Supporting information

Supplementary data associated with this article can be found in the online version at doi:10.1016/j.jcou.2024.102700.

References

[1] IPCC, AR6 Synthesis Report: Climate Change 2023 - IPCC, AR6 Synth. Rep. Clim. Chang. 2023 - IPCC. (2023). ⟨https://www.ipcc.ch/report/ar6/syr/⟩.

[2] R.M. Cuéllar-Franca, A. Azapagic, Carbon capture, storage and utilisation technologies: a critical analysis and comparison of their life cycle environmental impacts, J. CO2 Util. 9 (2015) 82–102, https://doi.org/10.1016/j.jcou.2014.12.001.

[3] A.A. Olajire, Recent progress on the nanoparticles-assisted greenhouse carbon dioxide conversion processes, J. CO2 Util. 24 (2018) 522–547, https://doi.org/10.1016/j.jcou.2018.02.012.

[4] C. Boschi, A. Dini, I. Baneschi, F. Bedini, N. Perchiazzi, A. Cavallo, Brucite-driven CO2 uptake in serpentinized dunites (Ligurian Ophiolites, Montecastelli, Tuscany), 264–281, Lithos (2017) 288–289, https://doi.org/10.1016/j.lithos.2017.07.005.

[5] P.B. Kelemen, J. Matter, In situ carbonation of peridotite for CO2 storage, Proc. Natl. Acad. Sci. U. S. A. 105 (2008) 17295–17300, https://doi.org/10.1073/pnas.0805794105.

[6] J.H. Kwak, J.Z. Hu, R.V.F. Turcu, K.M. Rosso, E.S. Ilton, C. Wang, J.A. Sears, M.H. Engelhard, A.R. Felmy, D.W. Hoyt, The role of H2O in the carbonation of forsterite in supercritical CO2, Int. J. Greenh. Gas. Control. 5 (2011) 1081–1092, https://doi.org/10.1016/j.ijggc.2011.05.013.

[7] M.J. McKelvy, A.V.G. Chizmeshya, J. Diefenbacher, H. Béarat, G. Wolf, Exploration of the role of heat activation in enhancing serpentine carbon sequestration reactions, Environ. Sci. Technol. 38 (2004) 6897–6903, https://doi.org/10.1021/es049473m.

[8] M.I. Rashid, E. Benhelal, F. Farhang, T.K. Oliver, M.S. Rayson, G.F. Brent, M. Stockenhuber, E.M. Kennedy, Development of Concurrent grinding for application in aqueous mineral carbonation, J. Clean. Prod. 212 (2019) 151–161, https://doi.org/10.1016/j.jclepro.2018.11.189.

[9] K. Rausis, A. Ćwik, Direct moist carbonation of brucite-rich serpentinized dunites: an alternative to the carbonation of heat-activated serpentine, Appl. Geochem. 127 (2021) 104851, https://doi.org/10.1016/j.apgeochem.2020.104851.

[10] I.M. Power, C. Paulo, H. Long, J.A. Lockhart, A.R. Stubbs, D. French, R. Caldwell, Carbonation, cementation, and stabilization of ultramafic mine tailings, Environ. Sci. Technol. 55 (2021) 10056–10066, https://doi.org/10.1021/acs.est.1c01570.

[11] A.L. Harrison, I.M. Power, G.M. Dipple, Accelerated carbonation of brucite in mine tailings for carbon sequestration, Environ. Sci. Technol. 47 (2013) 126–134, https://doi.org/10.1021/es3012854.

[12] A. Entezari Zarandi, F. Larachi, G. Beaudoin, B. Plante, M. Sciortino, Multivariate study of the dynamics of CO2 reaction with brucite-rich ultramafic mine tailings, Int. J. Greenh. Gas. Control. 52 (2016) 110–119, https://doi.org/10.1016/j.ijggc.2016.06.022.

[13] A.M. Chaka, A.R. Felmy, Ab initio thermodynamic model for magnesium carbonates and Hydrates, J. Phys. Chem. A. 118 (2014) 7469–7488, https://doi.org/10.1021/jp500271n.

[14] F.P. Glasser, G. Jauffret, J. Morrison, J.L. Galvez-Martos, N. Patterson, M.S.E. Imbabi, Sequestering CO2 by mineralization into useful nesquehonite-based products, Front. Energy Res. 4 (2016) 1–7, https://doi.org/10.3389/fenrg.2016.00003.

[15] L. Zhao, L. Sang, C. Jun, J. Ji, H.H. Teng, Aqueous carbonation of natural brucite: relevance to CO2 sequestration, Environ. Sci. Technol. 44 (2010) 406–411, https://doi.org/10.1021/es9017656.

[16] K.J. Fricker, A.H.A. Park, Investigation of the different carbonate phases and their formation kinetics during Mg(OH)2 slurry carbonation, Ind. Eng. Chem. Res. 53 (2014) 18170–18179, https://doi.org/10.1021/ie503131s.

[17] Y. Asakuma, M. Miura, Effect of microwave radiation on diffusion behavior of anti-solvent during crystallization, J. Cryst. Growth 402 (2014) 32–36, https://doi.org/10.1016/j.jcrysgro.2014.04.031.

[18] J. Gordon, H. Kazemian, S. Rohani, Rapid and efficient crystallization of MIL-53 (Fe) by ultrasound and microwave irradiation, Microporous Mesoporous Mater. 162 (2012) 36–43, https://doi.org/10.1016/j.micromeso.2012.06.009.

[19] H. Liu, K. Xiang, B. Yang, S. Yang, Q. Li, Microwave intensified synthesis of regular shaped sodium bisulfate crystal, Chem. Eng. Process. Process. Intensif. 95 (2015) 208–213, https://doi.org/10.1016/j.cep.2015.06.002.

[20] D.P. Serrano, M.A. Uguina, R. Sanz, E. Castillo, A. Rodríguez, P. Sánchez, Synthesis and crystallization mechanism of zeolite TS-2 by microwave and conventional heating, Microporous Mesoporous Mater. 69 (2004) 197–208, https://doi.org/10.1016/j.micromeso.2004.02.010.

[21] L. Li, Z. Guo, W. Han, Q. Wang, The effect of microwave on the primary nucleation of CaSO4 from aqueous solutions, Powder Technol. 317 (2017) 189–196, https://doi.org/10.1016/j.powtec.2017.03.051.

[22] J. Beiron, F. Normann, L. Kristoferson, L. Strömberg, S.Ò. Gardarsdòttir, F. Johnsson, Enhancement of CO2 Absorption in Water through pH Control and carbonic anhydrase-a technical assessment, Ind. Eng. Chem. Res. 58 (2019) 14275–14283, https://doi.org/10.1021/acs.iecr.9b02688.

[23] Z. Guo, W. Han, W. Zhao, L. Li, B. Wang, Y. Xiao, V. Alopaeus, The effect of microwave on the crystallization process of magnesium carbonate from aqueous solutions, Powder Technol. 328 (2018) 358–366, https://doi.org/10.1016/j.powtec.2018.01.038.

[24] R. Rodríguez-Clemente, J. Gómez-Morales, Microwave precipitation of CaCO3 from homogeneous solutions, J. Cryst. Growth 169 (1996) 339–346, https://doi.org/10.1016/S0022-0248(96)00389-2.

[25] A. Rizzuti, C. Leonelli, Crystallization of aragonite particles from solution under microwave irradiation, Powder Technol. 186 (2008) 255–262, https://doi.org/10.1016/j.powtec.2007.12.012.

[26] B.H. Toby, EXPGUI, a graphical user interface for GSAS, J. Appl. Crystallogr. 34 (2001) 210–213, https://doi.org/10.1107/S0021889801002242.

[27] R.A. Young, ed., The Rietveld Method, Oxford University Press, 1993 ISBN 0–19–855577–6.

[28] B. Lafuente, R.T. Downs, H. Yang, N. Stone, The power of databases: the RRUFF project. Highlights Mineral. Crystallogr, Walter de Gruyter GmbH, 2016, pp. 1–29, https://doi.org/10.1515/9783110417104-003. ISBN 9783110417104.

[29] F. Lucile, P. Cezac, F. Contamine, J.P. Serin, D. Houssin, P. Arpentinier, Solubility of carbon dioxide in aqueous solutions containing sodium hydroxide at pressure up to 4 MPa and temperature from 283 to 373 K: experimental measurement, J. Chem. Eng. Data. 57 (2012) 784–789, https://doi.org/10.1021/JE200991X.

[30] G. Giester, C.L. Lengauer, B. Rieck, The crystal structure of nesquehonite, MgCO3·3H2O, from Lavrion, Greece, Mineral. Petrol. 70 (2000) 153–163, https://doi.org/10.1007/s007100070001.

[31] M. Catti, G. Ferraris, S. Hull, A. Pavese, Static compression and H disorder in brucite, Mg(OH)2, to 11 GPa: a powder neutron diffraction study, Phys. Chem. Miner. 22 (1995) 200–206, https://doi.org/10.1007/BF00202300.

[32] M. Akao, S. Iwai, The hydrogen bonding of hydromagnesite, Acta Crystallogr. Sect. B. 33 (1977) 1273–1275, https://doi.org/10.1107/s0567740877005834.

[33] D.L. Graf, Crystallographic tables for the rhombohedral carbonates, Am. Mineral. 46 (1961) 1283–1316.

[34] G.W. Stephan, C.H. MacGillavry, The crystal structure of nesquehonite, MgCO3: 3H2O, Acta Crystallogr. Sect. B Struct. Crystallogr. Cryst. Chem. 28 (1972) 1031–1033, https://doi.org/10.1107/s0567740872003668.

[35] S. Lu, P. Yan, Y. Gao, C. Zhang, Theoretical Investigation of the energies, structures, and growth properties of hydromagnesite surfaces, Cryst. Growth Des. 20 (2020) 3722–3731, https://doi.org/10.1021/acs.cgd.9b01718.

[36] O. Qafoku, D.A. Dixon, K.M. Rosso, H.T. Schaef, M.E. Bowden, B.W. Arey, A.R. Felmy, Dynamics of Magnesite formation at low temperature and high pCO2 in aqueous solution, Environ. Sci. Technol. 49 (2015) 10736–10744, https://doi.org/10.1021/acs.est.5b02588.

[37] P. Dawson, C.D. Hadfield, G.R. Wilkinson, The polarized infra-red and Raman spectra of Mg(OH)2 and Ca(OH)2, J. Phys. Chem. Solids 34 (1973) 1217–1225, https://doi.org/10.1016/S0022-3697(73)80212-4.

[38] E.E. Coleyshaw, G. Crump, W.P. Griffith, Vibrational spectra of the hydrated carbonate minerals ikaite, monohydrocalcite, lansfordite and nesquehonite, Spectrochim. Acta - Part A Mol. Biomol. Spectrosc. 59 (2003) 2231–2239, https://doi.org/10.1016/S1386-1425(03)00067-2.

[39] H.G.M. Edwards, S.E.J. Villar, J. Jehlicka, T. Munshi, FT-Raman spectroscopic study of calcium-rich and magnesium-rich carbonate minerals, Spectrochim. Acta - Part A Mol. Biomol. Spectrosc. 61 (2005) 2273–2280, https://doi.org/10.1016/j.saa.2005.02.026.

[40] M.C. Hales, R.L. Frost, W.N. Martens, Thermo-Raman spectroscopy of synthetic nesquehonite - Implication for the geosequestration of greenhouse gases, J. Raman Spectrosc. 39 (2008) 1141–1149, https://doi.org/10.1002/jrs.1950.

[41] G. Raade, Dypingite, a new hydrous basic carbonate of magnesium, from Norway, Am. Mineral. 55 (1961) 1457–1465.

[42] A.L. Harrison, V. Mavromatis, E.H. Oelkers, P. Bénézeth, Solubility of the hydrated Mg-carbonates nesquehonite and dypingite from 5 to 35 °C: Implications for CO2 storage and the relative stability of Mg-carbonates, Chem. Geol. 504 (2019) 123–135, https://doi.org/10.1016/j.chemgeo.2018.11.003.

[43] P.J. Davies, B. Bubela, The transformation of nesquehonite into hydromagnesite, Chem. Geol. 12 (1973) 289–300.

[44] L. Hopkinson, P. Kristova, K. Rutt, G. Cressey, Phase transitions in the system MgO-CO2-H2O during CO2 degassing of Mg-bearing solutions, Geochim. Cosmochim. Acta 76 (2012) 1–13, https://doi.org/10.1016/j.gca.2011.10.023.

[45] K. Rausis, A. Ćwik, I. Casanova, Phase evolution during accelerated CO2 mineralization of brucite under concentrated CO2 and simulated flue gas conditions, J. CO2 Util. 37 (2020) 122–133, https://doi.org/10.1016/j.jcou.2019.12.007.

[46] H. Dong, C. Unluer, E.H. Yang, F. Jin, A. Al-Tabbaa, Microstructure and carbon storage capacity of hydrated magnesium carbonates synthesized from different sources and conditions, J. CO2 Util. 34 (2019) 353–361, https://doi.org/10.1016/j.jcou.2019.07.016.

[47] Q. Gautier, P. Bénézeth, V. Mavromatis, J. Schott, Hydromagnesite solubility product and growth kinetics in aqueous solution from 25 to 75°C, Geochim. Cosmochim. Acta 138 (2014) 1–20, https://doi.org/10.1016/j.gca.2014.03.044.

[48] Y. Lu, A. Sednev-Lugovets, P. Carvalho, M. Guzik, K. Dunkel, H. Austrheim, H. Friis, Dypingite series defined by the content of molecular H2O, Goldschmidt 2023 Conf. (2023). ⟨https://conf.goldschmidt.info/goldschmidt/2023/meetingapp.cgi/Paper/17096⟩.

[49] G. Yamamoto, A. Kyono, S. Okada, Thermal decomposition process of dypingite Mg5(CO3)4(OH)2·5H2O, Mater. Lett. 308 (2022) 131125, https://doi.org/10.1016/j.matlet.2021.131125.

[50] K. Huang, X. Yang, H. Zhu, Dynamics in Microwave Chemistry, Springer Nature Singapore Pte Ltd, 2021, https://doi.org/10.1007/978-981-15-9655-1.

[51] D. Azizi, F. Larachi, Surface speciation of brucite dissolution in aqueous mineral carbonation: insights from density-functional theory simulations, J. Phys. Chem. A. 123 (2019) 889–905, https://doi.org/10.1021/acs.jpca.8b09140.

[52] D. Toroz, F. Song, A. Uddin, G.A. Chass, D. Di Tommaso, A database of solution additives promoting Mg2+ dehydration and the onset of MgCO3 nucleation 22 (2022) 3080–3089, https://doi.org/10.1021/acs.cgd.1c01525.

[53] D. Toroz, F. Song, G.A. Chass, D. Di Tommaso, New insights into the role of solution additive anions in Mg^{2+} dehydration: implications for mineral

carbonation, CrystEngComm 23 (2021) 4896–4900, https://doi.org/10.1039/d1ce00052g.

[54] X. Zhang, P. Alvarez-Lloret, G. Chass, D. Di Tommaso, Interatomic potentials of Mg ions in aqueous solutions: structure and dehydration kinetics, Eur. J. Mineral. 31 (2019) 275–287, https://doi.org/10.1127/ejm/2019/0031-2815.